inorganics

MDPI

Article

Proton Conduction Properties of Intrinsically Sulfonated Covalent Organic Framework Composites

Jianjian Yang, Zhihui Kong, Xinyu Li, Qinglei Guo, Zhen Wang, Zixi Kang, Rongming Wang * and Daofeng Sun

State Key Laboratory of Heavy Oil Processing, School of Materials Science and Engineering, China University of Petroleum (East China), Qingdao 266580, China
* Correspondence: rmwang@upc.edu.cn

Abstract: The long–term stability of proton conductors is one of the most important factors in evaluating materials. Guest molecules can act as "bridges" for proton conduction channels and reside in the channels of covalent organic frameworks, but they are prone to leakage. Therefore, it is important to develop proton conductors with intrinsic proton conductivity. In this paper, we synthesized an intrinsically sulfonated covalent organic framework, TpPa–SO_3H, which has a more stable proton conducting performance than that of TpPa@H_2SO_4 by loading guest molecules. Meanwhile, the proton conductivity of TpPa–SO_3H was further improved by coating a superabsorbent polymer through an in situ reaction to obtain PANa@TpPa–SO_3H (PANa: sodium polyacrylate). As a result, the modified composite exhibits an ultrahigh proton conductivity of 2.33×10^{-1} S cm^{-1} at 80 °C under 95% relative humidity (RH). The stability of PANa@TpPa–SO_3H makes it an efficient proton transport platform with excellent proton conductivity and long–term durability.

Keywords: covalent organic framework; PANa; proton conduction; composite

Citation: Yang, J.; Kong, Z.; Li, X.; Guo, Q.; Wang, Z.; Kang, Z.; Wang, R.; Sun, D. Proton Conduction Properties of Intrinsically Sulfonated Covalent Organic Framework Composites. *Inorganics* **2023**, *11*, 283. https://doi.org/10.3390/inorganics11070283

Academic Editor: Tatjana N. Parac-Vogt

Received: 30 May 2023
Revised: 27 June 2023
Accepted: 29 June 2023
Published: 30 June 2023

1. Introduction

As economies grow and populations increase, various countries are experiencing increasing energy demand, leading to an increase in energy consumption [1]. The increasing energy consumption in countries around the world has put increasing pressure on the environment [2]. At present, fossil fuels (e.g., coal, oil, gas) are the main source of energy in the world and dominate the energy mix [3], while renewable energy sources such as solar and wind power still account for a small share of the total energy [4]. The combustion of fossil energy generates large amounts of pollutants and greenhouse gases, exacerbating global climate change and atmospheric pollution problems [5]. In order to solve these problems, scientists from various countries actively promote the development and utilization of sustainable new energy sources. New energy sources mainly include solar, wind, hydro, biomass, geothermal and hydrogen energy [6]. These energy sources have the advantages of being renewable, clean and low–pollution, which are important for promoting sustainable economic and social development and environmental protection [7].

Recently, the development of electrochemical energy technologies [8] has been increasingly accelerated due to its advantages of high efficiency, controllability and environmental protection. This technology is an important means to achieve sustainable energy development, and is mainly applied to energy storage and conversion, including lithium–ion batteries (LIB) [9], proton exchange membrane fuel cells (PEMFCs) [10], and electrochemical capacitors (EC) [11]. Among them, PEMFCs, as clean energy devices that generate electricity through electrochemical reactions, have good application prospects due to their mild working conditions and high energy conversion efficiency during operation [12]. As the core component of PEMFCs, the proton exchange membrane (PEM) directly affects the performance of the cells [13]. The ideal PEMs need to have low gas permeability,

high chemical and thermal stability, and good film formation capability in addition to high proton conductivity. The most commonly used commercially available proton exchange membranes are Nafion–based materials [14], which have a proton conductivity of 10^{-1} S cm^{-1} under high humidity conditions. However, Nafion membranes are complicated to synthesize, expensive, and have a narrow operating temperature range, so new materials need to be developed to replace them [15]. Currently, the development of fuel cell technology is mainly directed toward the development of proton–conducting materials with excellent overall performance.

Porous framework materials including hydrogen–bonded organic frameworks (HOFs) [16], metal–organic frameworks (MOFs) [17] and covalent organic frameworks (COFs) [18] have attracted great interest as proton–conducting materials [19]. Compared to HOFs and MOFs with certain drawbacks in stability, COFs linked by covalent bonds not only have a high specific surface area, adjustable pore size, and customizable structure and function, but also have high thermochemical stability and permanent porosity [20]. These characteristics sow their great advantages as emerging proton–conducting membrane materials [21], and make them widely investigated in fields such as chemical sensing, separation and photoelectric catalysis [22]. The porous nature of COFs provides the opportunity to load various guest molecules such as water, phosphoric acid, phytic acid, polymetallic oxides, and organic heterocyclic compounds into their channels, resulting in increasing studies in the field of proton conduction [23]. In terms of proton conduction, guest molecules present in the channels of COFs can serve as "bridges" for proton transfer to enhance their proton conduction performance [24]. However, most of the COFs do not possess intrinsic proton conductivity, and the guest molecules loaded in the channels are very prone to leakage [25], so it is important to develop COFs with intrinsic proton conductivity to ensure more stable proton conducting performance.

Herein, we describe a simple strategy to obtain stable COF composites with high proton conductivity by introducing acid groups and enriching water molecules as proton sources and carriers. The two COFs (TpPa and TpPa–SO_3H) with a similar structure except for the presence or absence of substituted sulfonic groups were synthesized in accordance with the previous reports [26,27], and then sulfuric acid (H_2SO_4) was loaded into the channels of TpPa to obtain TpPa@H_2SO_4 and compare its proton conducting stability with TpPa–SO_3H. As expected, TpPa@H_2SO_4 has poor proton conducting stability because of the leakage of H_2SO_4 from the channels of TpPa under humid conditions, but TpPa–SO_3H exhibits highly stable intrinsic proton conductivity. Subsequently, the water–absorbing polymer was coated on the surface of TpPa–SO_3H to enrich the water molecules in its channels. This not only enhanced the water retention capacity, but also promoted the formation of smooth proton transfer pathways, thus greatly improving the proton conductivity of TpPa–SO_3H. At 80 °C and under 95% RH, the proton conductivity of PANa@TpPa–SO_3H reached 2.33×10^{-1} S cm^{-1}, which can be compared with that of the excellent proton–conducting COF materials reported thus far; see Table S1.

2. Results and Discussion

TpPa and TpPa–SO_3H were synthesized using the solvothermal method via the reaction of 2,4,6–triformylphloroglucinol (Tp) with p–phenylenediamine (Pa) and 2,5–diaminobenzenesulfonic acid (Pa–SO_3H), respectively. TpPa@H_2SO_4 was prepared by grinding 85% H_2SO_4 into the channels, and PANa@TpPa–SO_3H was prepared by coating the water–absorbing polymer PANa on the surface of TpPa–SO_3H using an in situ reaction method. As shown in Figure S1a,b, Fourier transform infrared (FT–IR) spectra of TpPa and TpPa–SO_3H show the C=O stretching peak at 1643 cm^{-1} corresponding to the Tp disappears, and that no new C=O and N–H characteristic peaks appeared, while the typical stretching peaks attributed to the C=C and C–N bonds appeared at 1582 and 1253 cm^{-1}, respectively, indicating that they were successfully prepared and bore a keto–enamine linkage structure; see Scheme S1. Meanwhile, the peaks at 1026 and 1083 cm^{-1} attributed to symmetric and asymmetric O=S=O stretching bands in the IR spectrum of TpPa–SO_3H

confirm the presence of sulfonic acid groups. The phase purity of TpPa and TpPa–SO_3H was evaluated using powder x–ray diffraction (PXRD) and elemental analyses as shown in the synthesis part. The PXRD patterns of TpPa and TpPa–SO_3H show that they all have symmetric structures with typical AA–layer stacks, which were simulated using Materials Studio 2018; see Tables S2 and S3. The unit cell parameters of TpPa–SO_3H were a = b = 23.3 Å, c = 3.5 Å, and the peaks corresponding to the (100), (110), (120) and (001) faces appeared at 4.6°, 8.2°, 11.6° and 26.3°; see Figure S1c. Accordingly, the unit cell parameters were a = b = 23.3 Å, c = 3.8 Å, and the strong peak attributed to the (100), (110) and (001) crystal face appeared at 4.6°, 8.1° and 26.3°, respectively; see Figure S1d. Both TpPa and TpPa–SO_3H have good crystallinity. It can be clearly seen from the SEM images that TpPa and TpPa–SO_3H had a similar and regular strip–shaped form; see Figure S2a,c. TGA curves display that the two COFs were thermally stable before 300 °C; see Figure S3.

COFs have an excellent pore structure and large specific surface area, which can provide the directional assembly and orientation of guest molecules. The addition of guest molecules can modulate the chemical environment of COF channels to change proton density and proton conduction pathways and further improve its proton conduction efficiency. Therefore, their gas adsorption performance was also investigated using Brunauer–Emmett–Teller (BET) tests at 77 K; see Figure 1. The N_2 adsorption capacities of TpPa and TpPa–SO_3H were 213 and 145 $cm^3\ g^{-1}$, respectively, under 1 atm; see Figure 1a,b. It could be seen that the dense sulfonic acid groups made TpPa–SO_3H bear a smaller pore volume. Similarly, the calculated BET surface area of TpPa–SO_3H (78.9 $m^2\ g^{-1}$) was also smaller than that of TpPa (160.3 $m^2\ g^{-1}$). To verify the stability of the loaded guest molecules in the channels, TpPa@H_2SO_4 was obtained by introducing H_2SO_4 into the one–dimensional (1D) channels of TpPa. The gas adsorption test showed that the N_2 adsorption capacity of TpPa@H_2SO_4 decreased to 78 $cm^3\ g^{-1}$, and its pore size also decreased to 5.8 Å compared to the 15.5 Å pore size of TpPa; see Figure 1c. indicating that H_2SO_4 was successfully introduced into the channels of TpPa. This is also demonstrated by the IR tests; see Figure S4a. The O=S=O stretching bands at 1027, and 1081 cm^{-1} appeared in the spectrum of TpPa@H_2SO_4. ICP tests show that the mass content of sulfur (S) was 13.2%, which is equivalent to the 39.6% H_2SO_4 content in TpPa@H_2SO_4. The SEM images display that compared to that of TpPa, there was no significant change in the morphology of TpPa@H_2SO_4 (Figure S2b) and that TpPa@H_2SO_4 had good crystallinity as shown in the PXRD pattern (Figure S1c), indicating that the structure of TpPa remained stable after loading sulfuric acid. Subsequently, the proton conductivity tests of TpPa and TpPa@H_2SO_4 were performed at 80 °C via the impedance technique using their pressed pellets; see Figure S5a,b. The results show that TpPa had almost no proton conductivity until 60% RH, and had a conductivity of only 1.56×10^{-7} S cm^{-1} under 95% RH, while the corresponding value of TpPa@H_2SO_4 reached 1.33×10^{-1} S cm^{-1} under the same conditions; see Figure 2a,b and Figure S5a and Table S4. Compared to that of TpPa, the proton conductivity of TpPa@H_2SO_4 was improved by six orders of magnitude, which further confirms that H_2SO_4 was successfully introduced into the channels of TpPa.

However, the guest molecules loaded in the channels of COFs are usually unstable and prone to detachment, which will lead to the leakage of guest molecules and greatly reduce their proton conduction performance. Therefore, the stability of the proton conductivity of TpPa@H_2SO_4 was tested at 80 °C and 95% RH. The proton conductivity of TpPa@H_2SO_4 slightly decreased in the first three hours, but then decreased quickly; see Figure 2c. After testing for 12 h, the proton conductivity of TpPa@H_2SO_4 decreased to 82% of the original value. As demonstrated by the ICP test, the sulfur (S) content of TpPa@H_2SO_4 decreased to 10.7%, which is equivalent to 81% of the initial sulfur content. This result proves that there was a significant loss of H_2SO_4 molecules in the channels of COFs during the test, and the decrease in proton conductivity was proportional to the proportion of H_2SO_4 loss. Similarly, the proton conducting stability of TpPa–SO_3H was also tested at 80 °C; see Figure 2 and Table S4. Unlike TpPa, TpPa–SO_3H exhibited a moderate proton conductivity

of 3.65×10^{-5} only under 50% RH. When the humidity increased to 95%, the proton conductivity increased to 1.62×10^{-2} S cm^{-1}; see Figures 2a,b and S5c. After testing 12 h, the value remained at 1.56×10^{-2} S cm^{-1} (Figure 2d) which suggests it was almost unchanged considering the error factor. The ICP tests also revealed that the sulfur (S) content in TpPa–SO_3H was 10.5% before and after testing for 12 h, which is consistent with the theoretical sulfur content of 10.5%. These results indicate the stable intrinsic proton conduction nature and obvious humidity dependence of TpPa–SO_3H.

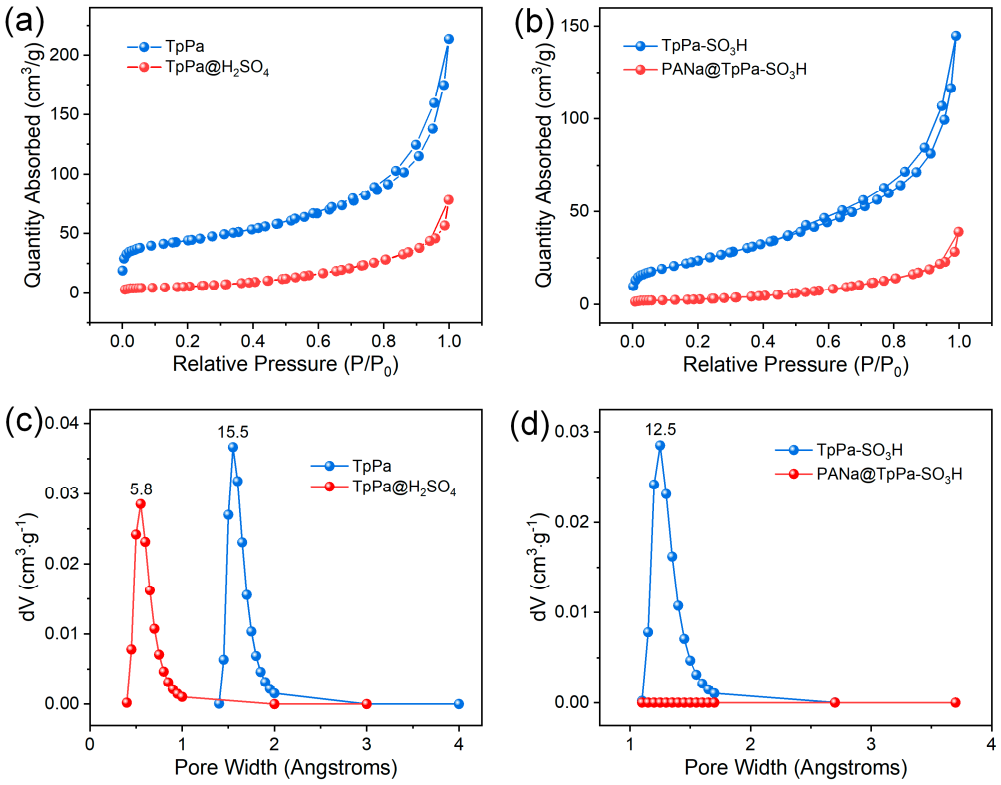

Figure 1. Nitrogen adsorption–desorption isotherms of TpPa and TpPa@H_2SO_4 (**a**), and TpPa–SO_3H and PANa@TpPa–SO_3H (**b**); pore size distribution of TpPa and TpPa@H_2SO_4 (**c**), and TpPa–SO_3H and PANa@TpPa–SO_3H (**d**).

The water storage capacity of proton conductors is important for the formation of smooth proton conduction pathways. In the proton conduction process, water molecules can not only serve as carriers for proton conduction, but can also dissociate and conduct protons through the following equilibrium: $H_2O = H^+ + OH^-$. Therefore, to further improve the water absorption and retention of TpPa–SO_3H and enhance its proton conduction performance, the highly absorbent polymer PANa was coated on the TpPa–SO_3H surface using an in situ reaction strategy to synthesize PANa@TpPa–SO_3H. Among them, PANa accounted for 40% of the by weight percentage of PANa@TpPa–SO_3H. According to the SEM images, PANa was well–coated on the surface of TpPa–SO_3H; see Figure S2d. The gas adsorption tests showed that the N_2 adsorption capacity of PANa@TpPa–SO_3H was only 39 cm^3 g^{-1}, which is much smaller than that of 145 cm^3 g^{-1} of TpPa–SO_3H; see Figure 1b. Meanwhile, it did not exhibit any pore size distribution; see Figure 1d. The results further indicate that the surface of TpPa–SO_3H was completely coated by PANa. To confirm this, the contact angle tests were performed on the JC2000 contact angle measuring instrument; see Figure 3. The results show that the angles of TpPa and TpPa–SO_3H were 78° and 21°, respectively. This indicates that the sulfonic acid groups existing in the channels of TpPa–SO_3H can effectively improve its hydrophilicity. However, PANa@TpPa–SO_3H exhibited complete wettability towards water, further showing that PaNa was successfully coated on the surface of TpPa–SO_3H, and that the hydrophilicity of TpPa–SO_3H

was improved after coating. Correspondingly, the humidity–dependent proton conductivity of PANa@TpPa–SO_3H was tested at 80 °C in the humidity range of 50–95%; see Figures 2a,b and S5c and Table S4. It can be seen that humidity has a significant effect on proton conduction. The proton conductivity of PANa@TpPa–SO_3H was 6.46×10^{-4} S cm^{-1} under 50% RH. When the humidity increased to 95%, the proton conductivity reached 2.33×10^{-1} S cm^{-1}, which is one order of magnitude higher than the corresponding value before coating, and close to the value of commercial Nafion membranes under the same conditions. Meanwhile, PANa@TpPa–SO_3H has excellent long–term durability as shown in Figure S8. This fully demonstrates the effectiveness of the coating strategy. Moreover, we also prepared PANa@TpPa and tested its proton conductivity, which only resulted in a proton conductivity of 8.9×10^{-2} S cm^{-1} at 80 °C and 95% RH, even though it also exhibited complete wettability towards water; see Figures 3c and S9. This further proves that the proton source provided by –SO_3H has an important effect on the proton conductivity.

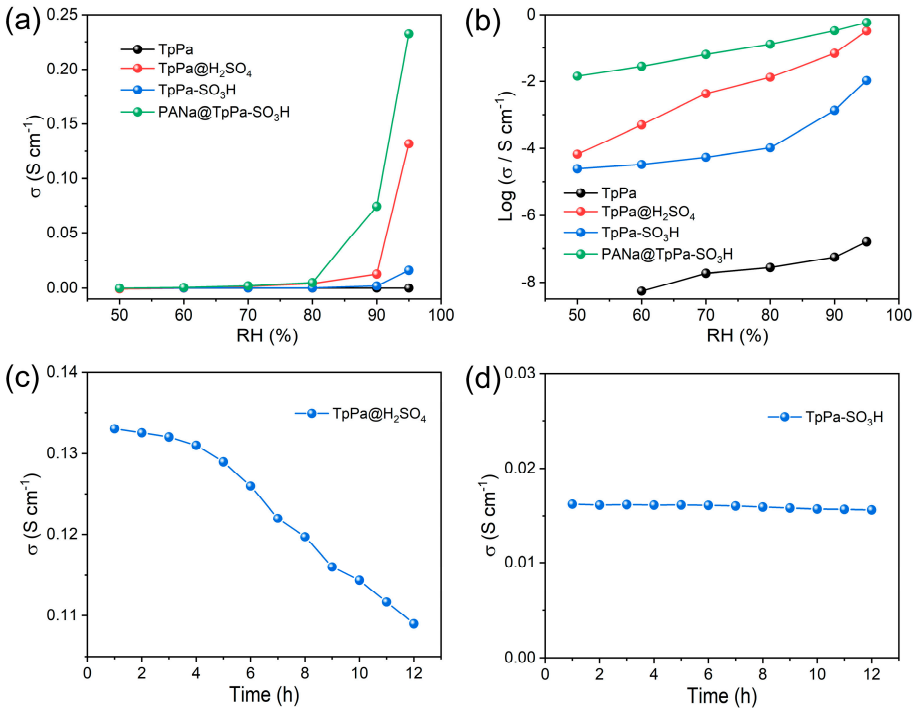

Figure 2. The humidity–dependent proton conductivities (**a**) and Log–scaled proton conductivities (**b**) of TpPa, TpPa@H_2SO_4, TpPa–SO_3H and PANa@TpPa–SO_3H; the time–dependent proton conductivities of TpPa@H_2SO_4 (**c**) and TpPa–SO_3H (**d**) at 80 °C under 95% RH.

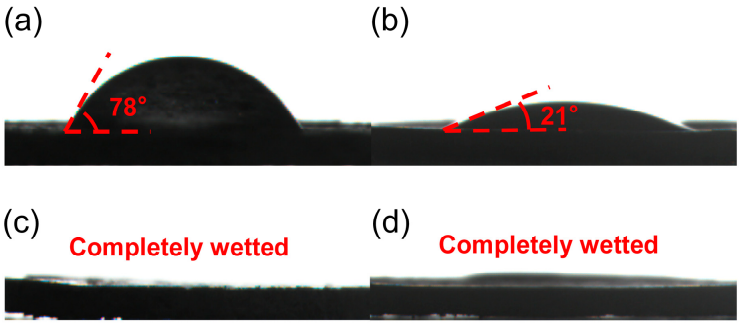

Figure 3. The contact angles of (**a**) TpPa, (**b**) TpPa–SO_3H, (**c**) PANa@TpPa and (**d**) PANa@TpPa–SO_3H.

To further understand the proton conduction mechanism, the temperature–dependent proton conductivity of TpPa, TpPa–SO_3H, and PANa@TpPa–SO_3H was studied; see

Figures 4, S6 and S7. The activation energies (E_a) obtained by fitting the temperature–dependent proton conductivity data for TpPa, TpPa–SO_3H and PANa@TpPa–SO_3H are 0.41, 0.30, and 0.26 eV, respectively, indicating that the proton transport in TpPa may adopt the mixed Grotthuss and vehicle mechanism, while the proton transport in TpPa–SO_3H and TpPa@H_2SO_4 and PANa@TpPa–SO_3H mainly adopts the Grotthuss mechanism. This is because there are no active protons in the channels of TpPa, and its proton conduction depends on the adsorbed water molecules. However, the water molecules serve as both proton carriers and proton resources. When the concentration of water molecules is not sufficient, they cannot form a large number of effective hydrogen–bonding networks, so some protons can only be transported through vehicle mechanisms. For strongly hydrophilic TpPa–SO_3H and PANa@TpPa–SO_3H, their channels not only possess active protons but also can enrich more water molecules as shown in contact angle test experiments, thus forming effective hydrogen bonding networks for transferring protons.

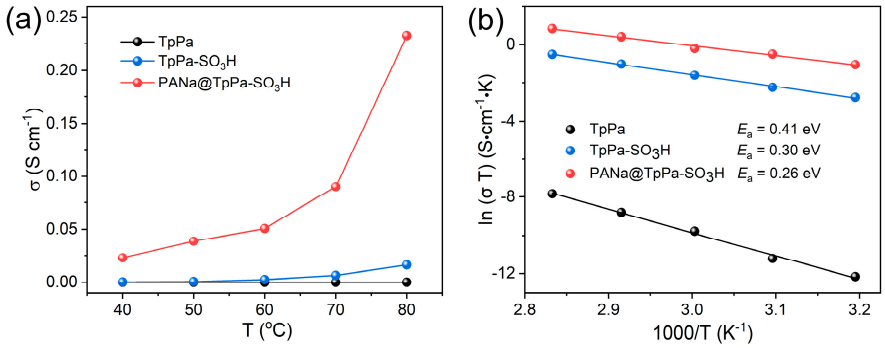

Figure 4. (**a**) Proton conductivities, and (**b**) Arrhenius plots of TpPa, TpPa–SO_3H and PANa@TpPa–SO_3H under different temperatures.

Both water absorption and swelling rate have important effects on the performance and stability of proton conductors. High water absorption and swelling rates may lead to reduced stability, mechanical properties and proton conduction efficiency, and affect the durability of proton conductors. Therefore, the water absorption and swelling rates of different ratios of PANa/TpPa–SO_3H were also studied in detail via direct weighing measurements after adsorbing water for 6 h at 80 °C and 95% RH; see Figure 5. It can be clearly seen that the water absorption and swelling rate of PANa@TpPa–SO_3H gradually increase with an increase in PANa content. Among them, the swelling rate of PANa@TpPa–SO_3H shows a linear relationship with its PANa content. When the PANa content was 40%, the water absorption capacity of PANa@TpPa–SO_3H reached 33.8% of its own weight and the swelling rate was 11.5%, which are values that are smaller than the corresponding values for commercial Nafion–based membranes. This indicates that PANa@TpPa–SO_3H is expected to be an ideal candidate for future commercialized materials.

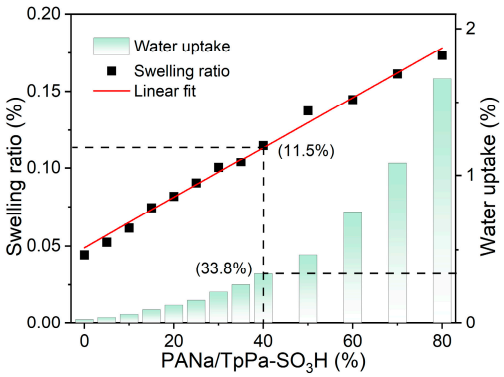

Figure 5. Water uptake and swelling ratio of different proportions of PANa@TpPa–SO_3H under 95% RH at 80 °C for 6 h.

3. Conclusions

In summary, we synthesized two COFs with and without sulfonate groups, demonstrating the instability of loaded guest molecules by introducing H_2SO_4 into the channels of TpPa. Meanwhile, the composite PANa@TpPa–SO_3H was constructed using an in situ reaction strategy. TpPa–SO_3H can provide orderly channels and bear active protons, and PANa can enrich water molecules into the channels of TpPa–SO_3H. After combining the advantages of both, PANa@TpPa–SO_3H possessed ultrahigh proton conductivity and a low swelling rate. This strategy provides a new approach for obtaining excellent COF–based proton–conducting materials with high stability and durability.

4. Materials and Methods

4.1. Materials

All the chemical reagents were commercially available and used without further purification. 2,4,6–Triformylphloroglucinol (99.9%), p–phenylenediamine (99.9%), and 2,5–diaminobenzenesulfonic acid (99.9%) were bought from Sigma Aldrich (shanghai, China). Ammonium persulphate (99%) was purchased from Sinopharm Chemical Reagent Co., Ltd., Shanghai, China. Acrylic acid (99%) and N,N′–methylene diacrylamide (99%) were supplied by Sahn Chemical Technology (Shanghai) Co., Ltd., Shanghai, China. Toluene, 1,4–dioxane, N,N–dimethylformamide, acetone, and ethanol were obtained from Tianjin Fuyu Fine Chemical Co., Ltd., Tianjin, China.

4.2. Synthesis Procedure

4.2.1. Preparation of TpPa

TpPa was synthesized in accordance with the method reported in the literature [26]. Briefly, 2,4,6–triformylphloroglucinol (21.0 mg, 0.1 mmol) and p–phenylenediamine (16 mg, 0.15 mmol) were dissolved in a 3 mL solution of mesitylene/1,4–dioxane (1/1) in a glass ampoule, to which 0.5 mL of 6 M acetic acid solution was added. The mixture was sonicated for 10 min, allowed to disperse uniformly, and then degassed in a liquid nitrogen bath using 3 freeze–pump–thaw cycles (vacuum < 50 mTorr). The tubes were sealed and then heated at 120 °C for 72 h to produce a light red solid at the bottom of the ampoule. After cooling to room temperature, the solvent was decanted and the solid was washed three times with N, N–dimethylformamide, acetone, and ethanol, respectively, and dried under dynamic vacuum at 120 °C for 10 h. The pale red powder was isolated in a 65% yield. The elemental analysis calculation for C_6ONH_4 revealed the following: C, 67.92; H, 3.80; N, 13.20; found: C, 67.98; H, 3.81; N, 13.19.

4.2.2. Preparation of TpPa@H_2SO_4

TpPa@H_2SO_4 was obtained by adding 85% of sulfuric acid (13 μL) into TpPa (10 mg), grinding it for half an hour. The sample was washed with a small amount of deionized water to remove the sulfuric acid on the surface of TpPa, and then dried under vacuum at 120 °C.

4.2.3. Preparation of TpPa–SO_3H

TpPa–SO_3H was synthesized in accordance with the method reported in the literature [27]. Briefly, 2,4,6–triformylphloroglucinol (21.0 mg, 0.1 mmol) and 2,5–diaminobenzenesulfonic acid (28 mg, 0.15 mmol) were dissolved in a 3 mL solution of mesitylene/1,4–dioxane (1/1) in a glass ampoule, to which 0.5 mL of 6 M acetic acid solution was added. The mixture was sonicated for 10 min, allowed to disperse uniformly, and then degassed in a liquid nitrogen bath using 3 freeze–pump–thaw cycles (vacuum < 50 mTorr). The tubes were sealed and then heated at 120 °C for 72 h to produce a red solid at the bottom of the ampoule. After cooling to room temperature, and the solid was washed three times with N, N–dimethylformamide, acetone, and ethanol, respectively, and dried under dynamic vacuum at 120 °C for 10 h. The red powder was isolated in 61% yield. for the elemental

analysis calculation revaled the following. $C_{13}O_5N_2H_8S$: C, 49.31; H, 2.76; N, 9.58; found: C, 49.28; H, 2.71; N, 9.59.

4.2.4. Preparation of PANa@TpPa and PANa@TpPa–SO_3H

Acrylic acid, ammonium persulphate, and N, N′–methylene diacrylamide were utilized as a monomer, initiator, cross–linker, respectively. Specifically, 3.6 mL of acrylic acid was mixed with 5 mL of deionized water to form solution A. An amount of 2 g of NaOH was dissolved in 5 mL of deionized water to form solution B. Solution B was added into solution A dropwise with stirring and ice bath cooling. Then, 55 mg of ammonium persulphate was added into the mixed solution, followed by the addition of 2 mg of N, N′–methylene diacrylamide.

An amount of 50 mg of ground TpPa–SO_3H was weighed on a glass slide, and the above mixed solution at 50 µL was added dropwise to TpPa–SO_3H and stirred well with a glass rod. Subsequently, a typical reaction of radical polymerization proceeded, and the mixture was placed in an oven at 65 °C for 2 h to allow PANa to grow in situ on TpPa–SO_3H. After the reaction was completed, the solid was washed with deionized water 3 times which to remove excess initiator, cross–linker and sodium hydroxide, then dried under dynamic vacuum at 65 °C for 2 h. The product was collected and weighed. PANa@TpPa was prepared with a similar procedure.

4.3. Proton Conductivity Measurement

The as–synthesized sample was placed in a mold and pressed into a pellet with a diameter of 3 mm (TpPa, TpPa@H_2SO_4, TpPa–SO_3H and PANa@TpPa–SO_3H) and a thickness range of 1–2 mm using a tableting machine. The pellet was placed in the center of the glass pellet and fixed horizontally with two 20 cm gold wires, two sides of the pellet were coated with silver glue, and we then waited for about 30 min for it to dry; see Figure S10. Impedance analysis was performed with 1260A Impedance/Gain–Phase Analyzer from 10 MHz to 0.1 Hz with an input voltage of 200 mV under constant temperature and humidity conditions, which were controlled using a BPS–50CL humidity control chamber. Each sample was pressed into at least three tablets, and repeated cyclic tests were performed on each tablet. Typically, the impedance at each temperature was measured after equilibration for a period of 6–10 h. The resistance values were obtained by fitting the impedance profile using zview software. The circuit equivalent used for fitting is as follows; see Figure 6:

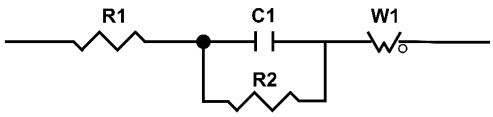

Figure 6. The circuit equivalent used for fitting.

R1 corresponds to the resistances of the wire and electrode, while R2 accounts for the bulk resistance of the pellet. The proton conductivity (σ, S cm^{-1}) of each sample was obtained via the following equation:

$$\sigma = \frac{l}{RS} \tag{1}$$

where l and S are the length (cm) and area (cm^2) of the pellet, respectively, and R is the intrinsic resistance value (Ω) of the material fitted by the equivalent circuit of the first semicircle using zview software. The activation energy (E_a) of the material is estimated according to the following Arrhenius equation:

$$\sigma T = \sigma_0 \exp\left(-\frac{E_a}{k_B T}\right) \tag{2}$$

where σ_0 is the pre–exponential factor, T is the temperature, and k_B is the Boltzmann constant.

4.4. Water Uptake and Swelling Ratio of PANa@TpPa–SO_3H Pellets

The pellet's water uptake was calculated from the weight difference between the dry pellet and wet pellet (Equation (3)), and their swelling ratios were tested by measuring the difference in length and thickness between the dry and wet pellets (Equation (4)). The dry and wet pellets were prepared with the same method as that used for proton conduction measurements.

$$\text{Water uptake}(\%) = 100 \times \frac{W_{wet} - W_{dry}}{W_{dry}} \quad (3)$$

$$\text{Swelling ratio}(\%) = 100 \times \frac{L_{wet} - L_{dry}}{L_{dry}} \quad (4)$$

where W_{dry} is the weight of the pellet dried in a vacuum until the weight is constant, and W_{wet} is the weight of the pellet placed under 95% RH and 80 °C for different durations.

4.5. Other Measurements

The date of powder X–ray diffraction (PXRD) was recorded on a Rigaku Ultima IV X–ray diffractometer with Cu–Kα radiation (l = 0.15418 nm). Diffraction patterns in the angle region (3–40°) were recorded at a rate of 2θ = 5°·min^{-1}. Thermal gravimetric analysis (TGA) was performed using the Mettler Toledo thermal analyzer with a heating rate of 10 °C min^{-1} in the range of 40–900 °C under a N_2 atmosphere. The water contact angle tests were carried out on the JC2000 contact angle measuring instrument. Elemental analysis was conducted on a PerkinElmer 240C elemental analyzer for C, H, and N determination. N_2 adsorption and desorption tests were performed on a Tristar 2460 surface area analyzer. Field–emission scanning electron microscopy (FESEM) images were obtained on a Hitachi SU–8000 instrument. The inductively coupled plasma mass (ICP–MS) spectra were recorded using an Optima 8000 spectrometer.

Supplementary Materials: The following supporting information can be downloaded at https://www.mdpi.com/article/10.3390/inorganics11070283/s1. Scheme S1: Synthesis of TpPa and TpPa–SO_3H, Figure S1: FT–IR spectra of (a) TpPa, p–phenylenediamine and 2,4,6–triformylphloroglucinol, (b) TpPa–SO_3H, 2,5–diaminobenzenesulfonic acid and 2,4,6–triformylphloroglucinol, (c) PXRD patterns of TpPa, TpPa@H_2SO_4 and PANa@TpPa, and (d) TpPa–SO_3H and PANa@TpPa–SO_3H. Figure S2: SEM image comparison of (a) TpPa, (b) TpPa@H_2SO_4, (c) TpPa–SO_3H, (d) PANa@TpPa, and (e) PANa@TpPa–SO_3H. Figure S3: Thermal gravimetric analysis of TpPa, TpPa@H_2SO_4, TpPa–SO_3H, and PANa@TpPa–SO_3H. Figure S4: FT–IR spectra of (a) TpPa and TpPa@H_2SO_4; (b) TpPa–SO_3H, PANa and PANa@TpPa–SO_3H; (c) TpPa, PANa and PANa@TpPa. Figure S5: Humidity–dependent proton conductivities at 80 °C; Nyquist plots of (a) TpPa, (b) TpPa@H_2SO_4, (c) TpPa–SO_3H, and (d) PANa@TpPa–SO_3H. Figure S6: Temperature–dependent Nyquist plots of (a) TpPa and (b) TpPa@H_2SO_4; (c) TpPa–SO_3H and (d) PANa@TpPa–SO_3H. Figure S7: Temperature–dependent Log–scaled proton conductivities of TpPa, TpPa@H_2SO_4, TpPa–SO_3H, and PANa@TpPa–SO_3H. Figure S8: The time–dependent proton conductivities of PANa@TpPa–SO_3H at 80 °C under 95% RH. Figure S9: Nyquist plots of PANa@TpPa at 80 °C under 95% RH. Figure S10: Proton conduction measurement diagram (a), and diameter and thickness of sample particles (b). Table S1: Comparison of proton conductivities in reported materials. Table S2: Fractional atomic coordinates for the unit cell of TpPa. Table S3: Fractional atomic coordinates for the unit cell of TpPa–SO_3H. Table S4: Humidity–dependent proton conductivity (S cm^{-1}) of TpPa, TpPa@H_2SO_4, TpPa–SO_3H, and PANa@TpPa–SO_3H. Table S5: Temperature–dependent proton conductivity (S cm^{-1}) of TpPa, TpPa@H_2SO_4, TpPa–SO_3H, and PANa@TpPa–SO_3H. References [28–44] are cited in the supplementary materials.

Author Contributions: Conceptualization, J.Y., Z.K. (Zixi Kang), R.W. and D.S.; Methodology, J.Y.; Validation, Z.W.; Investigation, R.W.; Resources, Z.K. (Zhihui Kong) and Q.G.; Data curation, J.Y.; Writing—original draft, J.Y.; Writing—review & editing, J.Y.; Visualization, R.W.; Supervision, X.L. All authors have read and agreed to the published version of the manuscript.

Funding: This work was supported by the National Natural Science Foundation of China (NSFC, grant no. 21771193, 22275210, 22201305), the Fundamental Research Funds for the Central Universities (22CX06024A), and the Outstanding Youth Science Fund Projects of Shandong Province (2022HWYQ–070).

Data Availability Statement: The data presented in this study are available upon request from the corresponding author.

Conflicts of Interest: The authors declare no conflict of interest.

Abbreviations

The following abbreviations are used in this manuscript:

LIB	Lithium–ion batteries
PEMFCs	Proton exchange membrane fuel cells
EC	Electrochemical capacitor
PEM	Proton exchange membrane
HOFs	Hydrogen–bonded organic frameworks
MOFs	Metal–organic frameworks
COFs	Covalent Organic Frameworks
FT–IR	Fourier transform infrared
BET	Brunauer−Emmett−Teller
RH	Relative humidity

References

1. Rode, A.; Carleton, T.; Delgado, M.; Greenstone, M.; Houser, T.; Hsiang, S.; Hultgren, A.; Jina, A.; Kopp, R.E.; McCusker, K.E.; et al. Estimating a Social Cost of Carbon for Global Energy Consumption. *Nature* **2021**, *598*, 308–314. [CrossRef]
2. Renn, O. Towards Climate Neutrality for Household Energy Consumption. *Natl. Sci. Rev.* **2022**, *9*, 83. [CrossRef]
3. Liu, J.; Huang, Z.; Fan, M.; Yang, J.; Xiao, J.; Wang, Y. Future Energy Infrastructure, Energy Platform and Energy Storage. *Nano Energy* **2022**, *104*, 107915. [CrossRef]
4. Palmer, G. Renewables Rise above Fossil Fuels. *Nat. Energy* **2019**, *4*, 538–539. [CrossRef]
5. Shih, C.F.; Zhang, T.; Li, J.; Bai, C. Powering the Future with Liquid Sunshine. *Joule* **2018**, *2*, 1925–1949. [CrossRef]
6. Gür, T.M. Review of Electrical Energy Storage Technologies, Materials and Systems: Challenges and Prospects for Large–Scale Grid Storage. *Energy Environ. Sci.* **2018**, *11*, 2696–2767. [CrossRef]
7. Li, X.; Jiang, C.; Ying, Y.; Ping, J. Biotriboelectric Nanogenerators: Materials, Structures, and Applications. *Adv. Energy Mater.* **2020**, *10*, 2002001. [CrossRef]
8. Wei, H.; Cui, D.; Ma, J.; Chu, L.; Zhao, X.; Song, H.; Liu, H.; Liu, T.; Wang, N.; Guo, Z. Energy Conversion Technologies Towards Self–Powered Electrochemical Energy Storage Systems: The State of the Art and Perspectives. *J. Mater. Chem. A* **2017**, *5*, 1873–1894. [CrossRef]
9. Ren, W.; Ding, C.; Fu, X.; Huang, Y. Advanced Gel Polymer Electrolytes for Safe and Durable Lithium Metal Batteries: Challenges, Strategies, and Perspectives. *Energy Storage Mater.* **2021**, *34*, 515–535. [CrossRef]
10. Fan, C.; Zhang, L.; Kong, Y.; Pang, X.; Gao, Z.; Wang, S.; Xing, N.; Wu, H.; Jiang, Z. Solid–State Synthesis of Intrinsically Proton–Conducting Covalent Organic Framework Membrane. *J. Membr. Sci.* **2023**, *676*, 121610. [CrossRef]
11. Fic, K.; Platek, A.; Piwek, J.; Frackowiak, E. Sustainable Materials for Electrochemical Capacitors. *Mater. Today* **2018**, *21*, 437–454. [CrossRef]
12. Xiao, F.; Wang, Y.C.; Wu, Z.P.; Chen, G.; Yang, F.; Zhu, S.; Siddharth, K.; Kong, Z.; Lu, A.; Li, J.C.; et al. Recent Advances in Electrocatalysts for Proton Exchange Membrane Fuel Cells and Alkaline Membrane Fuel Cells. *Adv. Mater.* **2021**, *33*, 2006292. [CrossRef] [PubMed]
13. Yang, J.; Xie, C.; Yang, Q.; Wang, S.; Gao, Y.; Ji, J.; Du, Z.; Kang, Z.; Wang, R.; Sun, D. PANa/Covalent Organic Framework Composites with Improved Water Uptake and Proton Conductivity. *Chem. Commun.* **2022**, *58*, 1131–1134. [CrossRef] [PubMed]
14. Patel, H.A.; Mansor, N.; Gadipelli, S.; Brett, D.J.; Guo, Z. Superacidity in Nafion/MOF Hybrid Membranes Retains Water at Low Humidity to Enhance Proton Conduction for Fuel Cells. *ACS Appl. Mater. Interfaces* **2016**, *8*, 30687–30691. [CrossRef]
15. Wang, J.; Li, P.; Zhang, Y.; Liu, Y.; Wu, W.; Liu, J. Porous Nafion Nanofiber Composite Membrane with Vertical Pathways for Efficient through–Plane Proton Conduction. *J. Membr. Sci.* **2019**, *585*, 157–165. [CrossRef]
16. Yang, Q.; Wang, Y.; Shang, Y.; Du, J.; Yin, J.; Liu, D.; Kang, Z.; Wang, R.; Sun, D.; Jiang, J. Three Hydrogen–Bonded Organic Frameworks with Water–Induced Single–Crystal–to–Single–Crystal Transformation and High Proton Conductivity. *Cryst. Growth Des.* **2020**, *20*, 3456–3465. [CrossRef]
17. Fan, W.; Wang, K.Y.; Welton, C.; Feng, L.; Wang, X.; Liu, X.; Li, Y.; Kang, Z.; Zhou, H.C.; Wang, R.; et al. Aluminum Metal–Organic Frameworks: From Structures to Applications. *Coord. Chem. Rev.* **2023**, *489*, 215175. [CrossRef]
18. Gong, Y.N.; Guan, X.; Jiang, H.L. Covalent Organic Frameworks for Photocatalysis: Synthesis, Structural Features, Fundamentals and Performance. *Coord. Chem. Rev.* **2023**, *475*, 214889. [CrossRef]

19. Wang, L.; Zhu, Y.; Du, C.; Ma, X.; Cao, C. Advances and Challenges in Metal–Organic Framework Derived Porous Materials for Batteries and Electrocatalysis. *J. Mater. Chem. A* **2020**, *8*, 24895–24919. [CrossRef]
20. Shinde, D.B.; Aiyappa, H.B.; Bhadra, M.; Biswal, B.P.; Wadge, P.; Kandambeth, S.; Garai, B.; Kundu, T.; Kurungot, S.; Banerjee, R. A Mechanochemically Synthesized Covalent Organic Framework as a Proton–Conducting Solid Electrolyte. *J. Mater. Chem. A* **2016**, *4*, 2682–2690. [CrossRef]
21. Shi, B.; Pang, X.; Lyu, B.; Wu, H.; Shen, J.; Guan, J.; Wang, X.; Fan, C.; Cao, L.; Zhu, T.; et al. Spacer–Engineered Ionic Channels in Covalent Organic Framework Membranes toward Ultrafast Proton Transport. *Adv. Mater.* **2023**, *35*, 2211004. [CrossRef]
22. Kang, C.; Zhang, Z.; Usadi, A.K.; Calabro, D.C.; Baugh, L.S.; Chai, K.; Wang, Y.; Zhao, D. Tunable Interlayer Shifting in Two–Dimensional Covalent Organic Frameworks Triggered by CO_2 Sorption. *J. Am. Chem. Soc.* **2022**, *144*, 20363–20371. [CrossRef] [PubMed]
23. Liu, R.; Wang, D.Y.; Shi, J.R.; Li, G. Proton Conductive Metal Sulfonate Frameworks. *Coord. Chem. Rev.* **2021**, *431*, 213747. [CrossRef]
24. Chandra, S.; Kundu, T.; Kandambeth, S.; Babarao, R.; Marathe, Y.; Kunjir, S.M.; Banerjee, R. Phosphoric Acid Loaded Azo (–N=N–) Based Covalent Organic Framework for Proton Conduction. *J. Am. Chem. Soc.* **2014**, *136*, 6570–6573. [CrossRef]
25. Dang, J.; Zhao, L.; Zhang, J.; Liu, J.; Wang, J. Imidazole Microcapsules toward Enhanced Phosphoric Acid Loading of Polymer Electrolyte Membrane for Anhydrous Proton Conduction. *J. Membr. Sci.* **2018**, *545*, 88–98. [CrossRef]
26. Zhong, W.; Sa, R.; Li, L.; He, Y.; Li, L.; Bi, J.; Zhuang, Z.; Yu, Y.; Zou, Z. A Covalent Organic Framework Bearing Single Ni Sites as a Synergistic Photocatalyst for Selective Photoreduction of CO_2 to CO. *J. Am. Chem. Soc.* **2019**, *141*, 7615–7621. [CrossRef]
27. Jeong, K.; Park, S.; Jung, G.Y.; Kim, S.H.; Lee, Y.H.; Kwak, S.K.; Lee, S.Y. Solvent–Free, Single Lithium–Ion Conducting Covalent Organic Frameworks. *J. Am. Chem. Soc.* **2019**, *141*, 5880–5885. [CrossRef]
28. Liu, L.; Yin, L.; Cheng, D.; Zhao, S.; Zang, H.Y.; Zhang, N.; Zhu, G. Surface-Mediated Construction of an Ultrathin Free-Standing Covalent Organic Framework Membrane for Efficient Proton Conduction. *Angew. Chem. Int. Ed.* **2021**, *60*, 14875–14880. [CrossRef]
29. Cao, L.; Wu, H.; Cao, Y.; Fan, C.; Zhao, R.; He, X.; Yang, P.; Shi, B.; You, X.; Jiang, Z. Weakly Humidity-Dependent Proton-Conducting COF Membranes. *Adv. Mater.* **2020**, *32*, 2005565. [CrossRef]
30. Yang, Y.; He, X.; Zhang, P.; Andaloussi, Y.H.; Zhang, H.; Jiang, Z.; Chen, Y.; Ma, S.; Cheng, P.; Zhang, Z. Combined Intrinsic and Extrinsic Proton Conduction in Robust Covalent Organic Frameworks for Hydrogen Fuel Cell Applications. *Angew. Chem. Int. Ed.* **2020**, *59*, 3678–3684. [CrossRef] [PubMed]
31. Zou, W.; Jiang, G.; Zhang, W.; Zhang, L.; Cui, Z.; Song, H.; Liang, Z.; Du, L. Hierarchically Macro–Microporous Covalent Organic Frameworks for Efficient Proton Conduction. *Adv. Funct. Mater.* **2023**, *15*, 2213642. [CrossRef]
32. Shao, Z.; Xue, X.; Gao, K.; Chen, J.; Zhai, L.; Wen, T.; Xiong, S.; Hou, H.; Mi, L. Sulfonated Covalent Organic Framework Packed Nafion Membrane with High Proton Conductivity for H_2/O_2 Fuel Cell Applications. *J. Mater. Chem. A* **2023**, *11*, 3446–3453. [CrossRef]
33. Wang, F.D.; Yang, L.J.; Wang, X.X.; Rong, Y.; Yang, L.B.; Zhang, C.X.; Yan, F.Y.; Wang, Q.L. Pyrazine-Functionalized Donor-Acceptor Covalent Organic Frameworks for Enhanced Photocatalytic H_2 Evolution with High Proton Transport. *Small* **2023**, *18*, 2207421. [CrossRef]
34. Wang, Z.; Yang, Y.; Zhao, Z.; Zhang, P.; Zhang, Y.; Liu, J.; Ma, S.; Cheng, P.; Chen, Y.; Zhang, Z. Green Synthesis of Olefin-Linked Covalent Organic Frameworks for Hydrogen Fuel Cell Applications. *Nat. Commun.* **2021**, *12*, 1982. [CrossRef] [PubMed]
35. Fu, Y.; Wu, Y.; Chen, S.; Zhang, W.; Zhang, Y.; Yan, T.; Yang, B.; Ma, H. Zwitterionic Covalent Organic Frameworks: Attractive Porous Host for Gas Separation and Anhydrous Proton Conduction. *ACS Nano* **2021**, *15*, 19743–19755. [CrossRef] [PubMed]
36. Wu, X.; Hong, Y.L.; Xu, B.; Nishiyama, Y.; Jiang, W.; Zhu, J.; Zhang, G.; Kitagawa, S.; Horike, S. Perfluoroalkyl-Functionalized Covalent Organic Frameworks with Superhydrophobicity for Anhydrous Proton Conduction. *J. Am. Chem. Soc.* **2020**, *142*, 14357–14364. [CrossRef]
37. Chen, S.; Wu, Y.; Zhang, Y.; Zhang, W.; Fu, Y.; Huang, W.; Yan, T.; Ma, H. Tuning Proton Dissociation Energy in Proton Carrier Doped 2D Covalent Organic Frameworks for Anhydrous Proton Conduction at Elevated Temperature. *J. Mater. Chem. A* **2020**, *8*, 13702–13709. [CrossRef]
38. Samanta, P.; Desai, A.V.; Anothumakkool, B.; Shirolkar, M.M.; Karmakar, A.; Kurungot, S.; Ghosh, S.K. Enhanced Proton Conduction by Post-Synthetic Covalent Modification in a Porous Covalent Framework. *J. Mater. Chem. A* **2017**, *5*, 13659–13664. [CrossRef]
39. Peng, Y.; Xu, G.; Hu, Z.; Cheng, Y.; Chi, C.; Yuan, D.; Cheng, H.; Zhao, D. Mechanoassisted Synthesis of Sulfonated Covalent Organic Frameworks with High Intrinsic Proton Conductivity. *ACS Appl. Mater. Interfaces* **2016**, *8*, 18505–18512. [CrossRef]
40. Jiang, G.; Zou, W.; Ou, Z.; Zhang, L.; Zhang, W.; Wang, X.; Song, H.; Cui, Z.; Liang, Z.; Du, L. Tuning the Interlayer Interactions of 2D Covalent Organic Frameworks Enables an Ultrastable Platform for Anhydrous Proton Transport. *Angew. Chem. Int. Ed.* **2022**, *61*, 202208086. [CrossRef]
41. Guo, Z.C.; You, M.L.; Wang, Z.J.; Li, Z.F.; Li, G. Metal@Cofs Possess High Proton Conductivity with Mixed Conducting Mechanisms. *ACS Appl. Mater. Interfaces* **2022**, *14*, 15676–15687. [CrossRef]
42. Meng, Z.; Aykanat, A.; Mirica, K.A. Proton Conduction in 2D Aza-Fused Covalent Organic Frameworks. *Chem. Mater.* **2018**, *31*, 819–825. [CrossRef]

43. Ma, H.; Liu, B.; Li, B.; Zhang, L.; Li, Y.G.; Tan, H.Q.; Zang, H.Y.; Zhu, G. Cationic Covalent Organic Frameworks: A Simple Platform of Anionic Exchange for Porosity Tuning and Proton Conduction. *J. Am. Chem. Soc.* **2016**, *138*, 5897–5903. [CrossRef] [PubMed]
44. Chandra, S.; Kundu, T.; Dey, K.; Addicoat, M.; Heine, T.; Banerjee, R. Interplaying Intrinsic and Extrinsic Proton Conductivities in Covalent Organic Frameworks. *Chem. Mater.* **2016**, *28*, 1489–1494. [CrossRef]